Supplementary material: Strong chiral dichroism and enantio-purification in above threshold ionization with locally-chiral light

Ofer Neufeld[1,2,*], Hannes Hübener[1], Angel Rubio[1,3], Umberto De Giovannini[1,4]

[1]Max Planck Institute for the Structure and Dynamics of Matter, Hamburg, Germany, 22761.
[2]Physics Department and Solid State Institute, Technion - Israel Institute of Technology, Haifa, Israel, 32000.
[3]Center for Computational Quantum Physics (CCQ), The Flatiron Institute, New York, NY, USA, 10010.
[4]IKERBASQUE, Basque Foundation for Science, E-48011, Bilbao, Spain.

I. METHODS

Ab-initio calculations. All DFT calculations were performed using the octopus code[41–43]. The Kohn Sham (KS) equations were discretized on a Cartesian grid with spherical boundaries of radius 45 bohr, where molecular center of masses were centered at the origin. Calculations were performed using the local density approximation (LDA) with an added self-interaction correction (SIC)[55]. This is a crucial point as adding the SIC guarantees a correct long-range KS potential that decays non-exponentially, and is required to obtain correct PECD[44]. The frozen core approximation was used for inner core orbitals, which were treated with appropriate norm-conserving pseudopotentials[56]. The KS equations were solved to self-consistency with a tolerance $<10^{-7}$ Hartree, and the grid spacing was converged to $\Delta x=\Delta y=\Delta z=0.4$ bohr, such that the total energy per electron was converged $<10^{-3}$ Hartree. All molecular structures were relaxed $<10^{-4}$ Hartree/bohr in forces within the LDA.

For time-dependent calculations in the SAE approximation, the HOMO KS orbital was propagated with a time step $\Delta t=0.105$ a.u. (deeper levels were frozen), and by adding an imaginary absorbing potential of width 15 bohr at the boundary. The initial state was taken to be the system's ground-state. The propagator was represented by an 8th order Taylor expansion. The grid size, absorbing potential, and time step were tested for convergence. For the full TDDFT calculations presented in the SM the same approach was utilized, but where all valence electrons were propagated in tandem and the KS potential was updated in every temporal iteration. For the multi-electron calculations with frozen dynamical correlations presented in the SM, again all valence electrons were propagated, but where the KS potential was frozen in time to its ground state form (i.e. that arising from the ground state electron density).

Photoelectron chiral dichroism and ATI spectra. The full PES from each molecular orientation was calculated using the t-surff method[45,46], implemented within the octopus code[47–49]. A spherical surface where flux was calculated was positioned at $r=30$ bohr, where integration was performed with a maximal angular momentum index for spherical harmonics of 40, angular grids were spanned with spacing 1º, k-grids were spanned with a spacing of $\Delta k=2\times10^{-3}$ a.u. and up to a maximal energy of 75 eV. The orientation averaged PES was calculated by trapezoidal integration as specified below, where the laser axes were repositioned and oriented with rotation matrices, and the PES was interpolated using cubic splines on the rotated grids. Photoelectron chiral dichroism spectra were obtained directly by subtracting the PES calculated from mirror image enantiomers. Integration over Cartesian axes and angular grids was performed using Simpson integration. The total ionization rate was calculated directly from the electron density rather than integration over the ATI spectra, since this approach has improved accuracy.

Orientation averaging. Orientation averaging was performed by spanning the angular grid with Euler angles in the z-y-z convention. The three Euler angles were spanned on equidistant grids with spacing $\pi/4$, leading to a total of 405 orientations and 208 irreducible orientations. Summation was performed with trapezoidal weights. The angular grid was converged against a twice reduced grid in the second Euler angle (leading to a total of 729 orientations and 464 irreducible orientations), converging the maximal ATI chiral dichroism by 0.71% and the total ionization rate dichroism by 0.55%.

II. ADDITIONAL RESULTS FROM CBRCLFH

We present here additional results of calculations performed for CBrClFH that are complementary to the results presented in the main text.

First, we present PECD spectra for the CPL case (see Fig. S1), i.e. after setting α=0, Δ=0, ε_1=1 in eq. (1) in the main text, and after setting the laser power to $I_0=4\times10^{13}$ W/cm^2 to have the same total power as in calculations presented in the main text. Results show an almost perfect forwards/backwards asymmetry, as expected, with symmetric parts constituting <0.01%. The chiral dichroism reaches the highest value of 2.01% for 800nm driving and 5.05% for 400nm driving, which is smaller than when using locally-chiral light as shown in the main text. The value of 5.05% at 400nm appears only in the low energy part of the spectrum and results from a largely perturbative interaction which is known to lead to lager PECD signals. In that sense, in the high energy parts the use of chiral light still leads to almost a factor 5-10 increase in the PECD. Additionally, PECD in the *xz* and *yz* planes are almost identical, and present almost perfect up/down left/right symmetries. Deviation from up/down and left/right symmetry is a result of the short laser pulse duration, which are carrier-envelope phase (CEP) dependent quantities. We emphasize that the effects of CEP here are smaller than 1%. Moreover, for our particular choice of pulse the integral over the vector potential is zero such that CEP effects contribute negligibly to the chiral dichroism obtained with locally-chiral light (this is also apparent in the ATI spectra that exhibit sharp peaks rather than a continuous emission). We further verified that for the CPL case the PECD in the *xy* plane is <10^{-3}%, the ATI chiral dichroism is <2×10^{-3}%, and the total ionization rates chiral dichroism is <2×10^{-4}%. These results constitute a sanity check for the convergence of the angular grid, and for the appropriateness of the numerical approach.

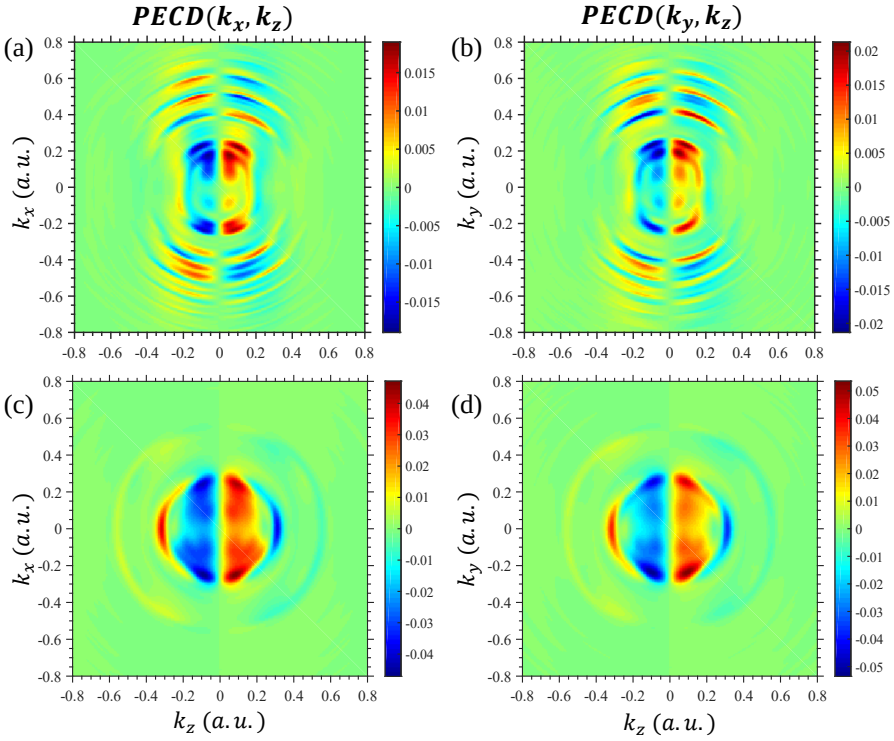

FIG. S1. PECD using CPL from CBrClFH. Calculations are performed by substituting α=0, Δ=0, ε_1=1 in eq. (1), and setting the laser power to $I_0=4\times10^{13}$W/cm^2 (in (a)-(b)), or $I_0=2\times10^{13}$W/cm^2 (in (b)-(c)), such that the total power is equal to that in Figure 2 in the main text that uses ω-2ω. (a-b) PECD for 800nm carrier wavelength. (c-d) PECD for 400nm carrier wavelength. Note that the color scales are different in all sub-plots and range from the minimal to maximal values of dichroism in each case.

Next, we present ATI chiral dichroism calculations obtained from a higher laser power of $I_0=4\times10^{13}$W/cm^2, as compared to results in Fig. 3 in the main text. Figure S2 presents the ATI chiral dichroism and generally shows a stronger dichroism with a maximal value of 7.04%. Note that even though the maximal value of the ATI discrimination is larger, the total ionization rate discrimination here is 0.31%, which is lower than its value of 2.46% at the lower laser power because the ATI chiral dichroism is more oscillatory and changes sign between different ATI peaks. This is an indication that it is not necessarily straightforward that higher laser powers directly lead to stronger chiral signals. We note that by selectively removing photoelectrons with low energies (or high energies) one can artificially increase the total ionization rates chiral dichroism.

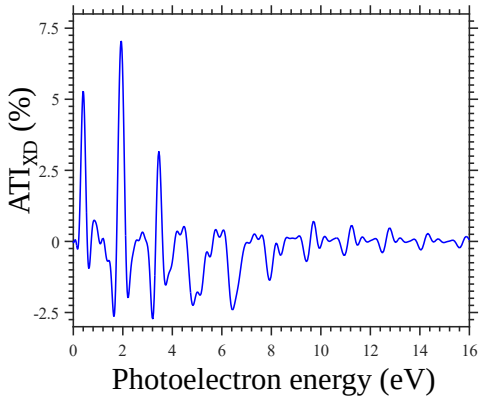

FIG. S2. ATI chiral dichroism from CBrClFH at a higher laser power. Calculations are performed in similar ω-2ω optical beam settings to those in Fig. 3, but with a larger laser power of $I_0=4\times10^{13}$W/cm^2.

Lastly, we address the use of the single active electron (SAE) approximation in the main text and throughout our analysis. We test this approximation by directly solving the full TDDFT equations including all active electrons in similar settings to those analyzed in the main text in Figs. 2 and 3. Results are presented in Fig. S3 for two separate cases: (a-d) including or (e-h) excluding dynamical *e-e* interactions in the calculation. Here two main results can be highlighted: (i) while the quantitative values of chiral dichroism obtained in the SAE approximation vary from those obtained with the full calculation, the qualitative nature of our approach remains the same. That is, antisymmetric Photoelectron chiral dichroism is observed in all hemispheres with values reaching several percent, which survive orientation averaging. Notably, the absolute values of dichroism are reduced in the multi-electron calculation by a factor of 2-3, which can be explained by contributions to ionization from deeper states that constitute an achiral background. We expect that by optimizing the laser power and wavelength such that only the HOMO orbital contributes dominantly, the dichroism can be further improved. (ii) Both multi-orbital interference and dynamical *e-e* interactions play a crucial role in the quantitative description of strong-field ionization in this regime. This is obvious by comparing results in Figs. S3(a-d) to those in the main text, and to those in Fig. S3 (e-h). *e-e* interactions seem to reduce the absolute chiral dichroism values. The mechanism for this effect remains to be investigated, but could potentially be used to probe dynamical correlations with PES.

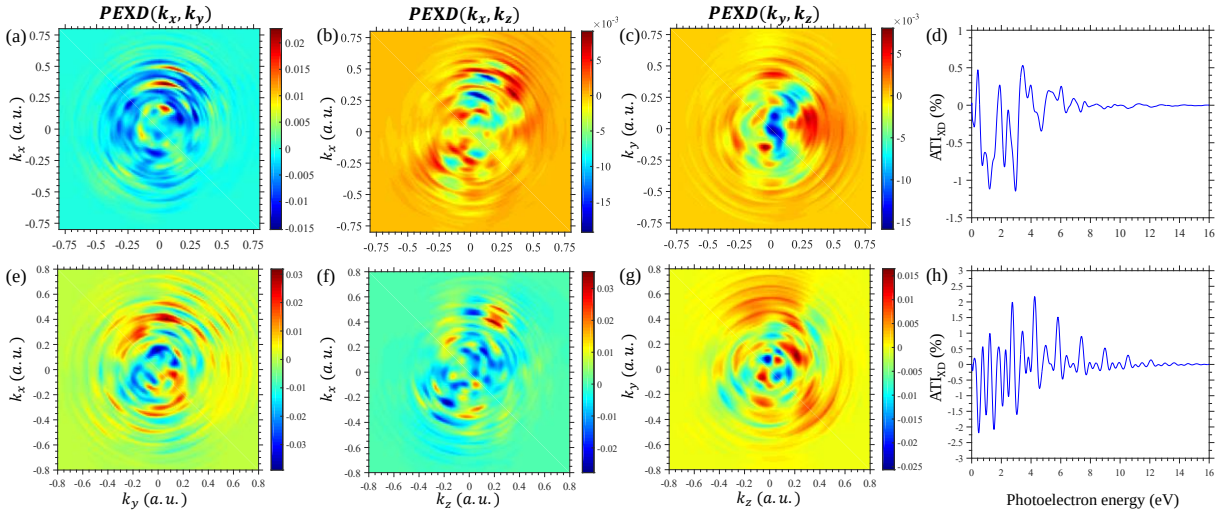

FIG. S3. Photoelectron chiral dichroism and ATI chiral dichroism from CBrClFH from multi-electron TDDFT calculations. (a-d) Results from the full TDDFT calculation. (e-h) Results from the multi-electron calculation where dynamical correlations have been frozen by freezing the KS potential to its initial form. Calculations are performed in similar ω-2ω optical beam settings to those in Figures 2 and 3 in the main text. Note that the color scales are different in all sub-plots and range from the minimal to maximal values of dichroism in each case.

III. ADDITIONAL RESULTS FROM LIMONENE, FENCHONE, AND CAMPHOR

We present here additional results from the chiral molecules Limonene, Fenchone, and Camphor. Figure S4 presents the Photoelectron chiral dichroism in all hemispheres calculated for these molecules in the same

settings as Fig. 5 in the main text. Limonene here shows the strongest chiral dichroism, in accordance with the ATI chiral dichroism presented in Fig. 5.

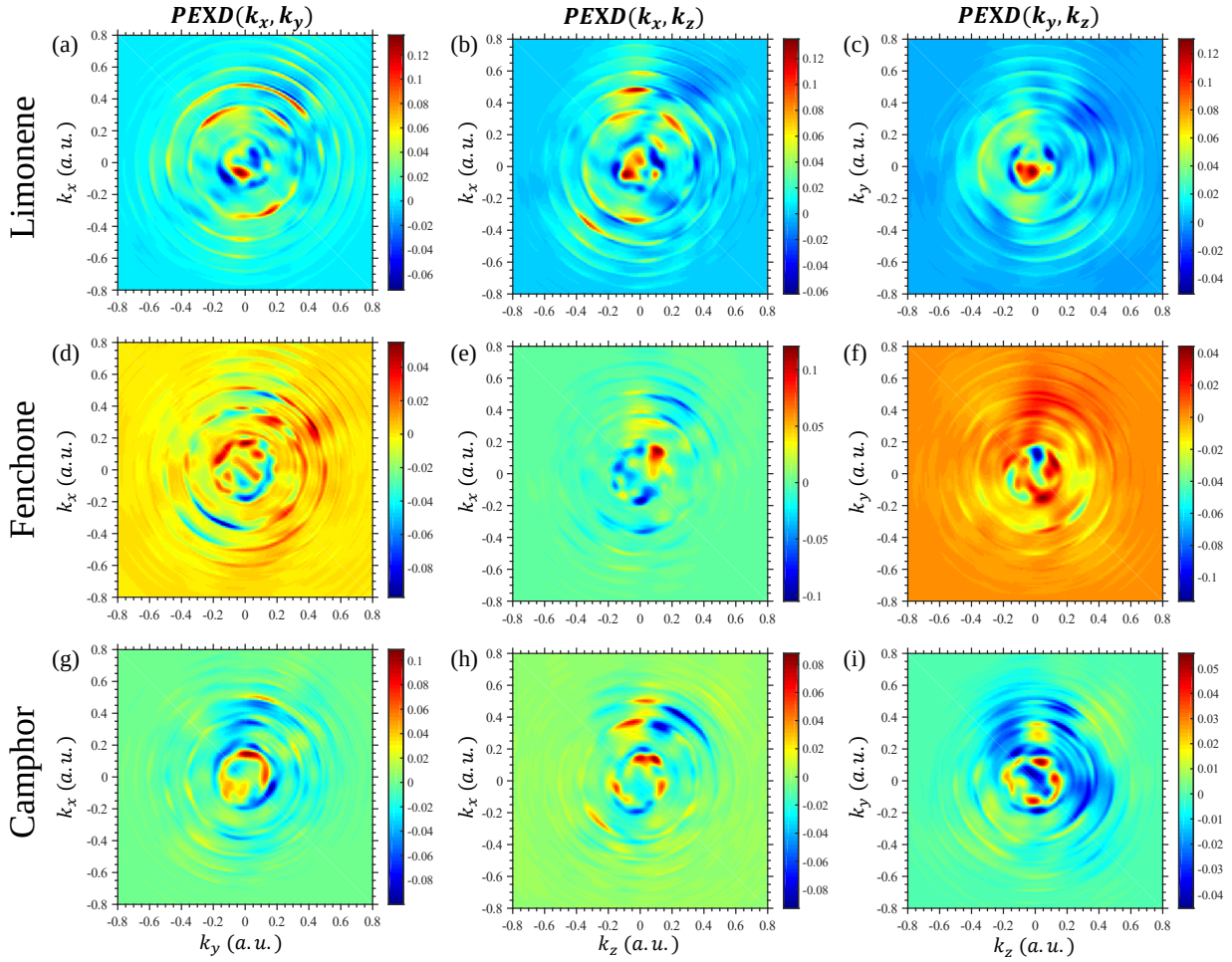

FIG. S4. Photoelectron chiral dichroism spectra from (a-c) Limonene, (d-f) Fenchone, (g-i) Camphor, respectively. Calculations are performed in similar ω-2ω optical beam settings to those in Figure 5 in the main text. Note that the color scales are different in all sub-plots and range from the minimal to maximal values of dichroism in each case.